Chapter 11
Single Molecule Force Spectroscopy

Rémy Pawlak, Shigeki Kawai, Thilo Glatzel and Ernst Meyer

Abstract Molecular-scale forces has a pivotal role in biological, chemical and physical processes. *Single molecule force spectroscopy* refers to the study of these forces as well as the mechanical properties of single molecules under applied forces. The term has appeared more than two decades ago in the field of biochemistry, however the recent advances of atomic force microscopy (AFM) operated at low temperature have brought such studies down to the atomic level hence opening new exciting perspectives. At this ultimate level, the intrinsic properties of individual organic species are now quantified by measuring force and conductance informations at the sub-molecular level. Not only restricted to the mechanics of the adsorbates, these techniques are nowadays employed to reveal their chemical structures, their electronic characteristics as well as their optical properties. This chapter reviews proto-typical experiments revealing the fundamental properties of single molecules using advanced spectroscopic techniques at low temperature. First, we will discuss the requirements of such spectroscopic experiments as well as the "essence" of the physical quantities extracted from them. Section 11.3 will respectively show the capability of this approach in the elucidation of the structure of single molecules, the mechanical properties, their internal mechanical behavior under various manipulation processes. Section 11.4 will be dedicated to the study of their electronic and optical properties down to the sub-molecular scale. Finally, Sect. 11.5 will discuss the future prospects.

R. Pawlak (✉) · S. Kawai · T. Glatzel · E. Meyer
Department of Physics, University of Basel, Klingelbergst. 82, 4056 Basel, Switzerland
e-mail: remy.pawlak@unibas.ch

S. Kawai
e-mail: shigeki.kawai@unibas.ch

T. Glatzel
e-mail: thilo.glatzel@unibas.ch

E. Meyer
e-mail: ernst.meyer@unibas.ch

S. Morita et al. (eds.), *Noncontact Atomic Force Microscopy*,
NanoScience and Technology, DOI 10.1007/978-3-319-15588-3_11

11.1 Introduction: Towards Single Molecule Investigations with nc-AFM

Since the development of scanning tunneling microscopy (STM) by Bining et al. [1] and shortly after atomic force microscopy (AFM) [2], exploring and interacting with surfaces with atomic precision is a dream became true [3, 4]. Looking at atoms as well as molecules with such techniques has rapidly opened a widespread interest in various scientific field such as material science, engineering, fundamental physics, chemistry and biology.

Following the first atomic resolution by non-contact atomic force microscopy (ncAFM) [6–8], the technique has proven its ability for observing with atomic resolution metallic [9, 10], semiconducting [6, 8, 11, 12] and insulating surfaces [13–15]. In addition to "see" atoms, many efforts have been focused by the community to quantify forces arising between the interaction of the AFM tip and various surfaces by conducting spectroscopic measurements [16–22]. The remarkable advances in understanding and acquiring these data have then shown the capability of the technique to chemically identify atomic species at surfaces [24–26], manipulate atoms in a controlled way [27–29] or build-up 2D- and 3D-force vector fields with atomic-scale precision [31–35]. An additional benefit of such spectroscopic approaches compared to imaging is the recovery of the normal and lateral forces as well as the potential energy landscape of the tip-sample interactions via post-processing [32, 36–39] which reveal the AFM technique as a unique tool for characterizing forces at the atomic scale.

If real-space observations of single molecules by STM appeared in the early 90's [40], such achievements with ncAFM were slightly delayed [41–44] principally due to the need of technological improvements. For instance, studies of single molecules via force spectroscopy using a silicon cantilever appeared in 2003 with the mechanical switching of a single porphyrin molecule [45] or the observation of single nanotubes with atomic precision [46]. The implementation of quartz tuning forks as force sensor (qPlus sensor [47–49]) brought the ncAFM mode even further by allowing unique experiments combining force and current detection at low temperature. In 2009, the resolution of the chemical structure of a single molecule was demonstrated by L. Gross and coworkers by means of direct imaging and 3D-force spectroscopy [50]. The charge state of single adatoms, point defects in MgO and single molecules on NaCl thin films were also determined by mapping the local potential difference (LCPD) between tip and sample [51–54], a technique which was also employed to reveal the charge distribution within single molecules [55–58]. Further experiments based on force and current spectroscopies were then widely used to understand molecular properties and physical phenomena at the nanoscale [59–69].

Single molecule force spectroscopy reveals the mechanical response of individual molecules under localized forces applied and measured with an AFM. With the latest advances in spectroscopic techniques combining force and current, it is now also possible to reveal their chemical structure, their electronic properties (electronic gap, charge state, internal dipole moment) down to the sub-molecular scale.

In this chapter, we will introduce our recent works on force spectroscopy performed on individual molecules at low temperature. We will briefly discuss experimental requirements such as the isolation of molecules, the precise data acquisition of force and current spectroscopic information simultaneously and their post-processing. Then, we will show the investigation of the structural and mechanical properties of single organic species at the sub-molecular scale as well as their mechanical behaviour during vertical or lateral manipulation with the AFM tip. A second section will focus on combined spectroscopic measurements of force and current giving important insights into the electronic properties of single molecules. Finally, we will discuss future experimental considerations and experiments to observe new physical phenomena at this ultimate level.

11.2 Experimental Requirements

11.2.1 Single Molecules at Surfaces

Performing single molecule force spectroscopy experiments requires the isolation of the organic species on top of atomically cleaned surfaces. Substrates, typically crystal facets of Cu, Ag, and Au, are prepared by several cycles of sputtering/annealing in ultrahigh vacuum. Evaporated from a Knudsen cell heated up to the sublimation temperature of the molecule, the organic species usually possess sufficient amount of kinetic energy to diffuse on the surface at room temperature leading to step adsorption or self-assembly. The molecule-surface interaction has a fundamental role in controlling the diffusion length of the organic species. When adsorbed on reactive metals or semi-conductors having dangling bonds isolated molecules can be found at room temperature, however it is usually not the case when deposited on bulk insulators at room temperature.

A "trick" to overcome this issue introduced by Repp et al. [70, 71] is to conduct such evaporations within the microscope at low temperature (4.8 K) to avoid diffusion. In this way and as depicted in Fig. 11.1, molecules are usually isolated and randomly distributed on the surface while its adsorption geometry is determined by the molecule-substrate interaction. In addition, ultrathin films of an insulating materials such as NaCl can be grown on these metal surfaces to be used as decoupling layers. Molecules deposited on top of them are electronically decoupled from the metals

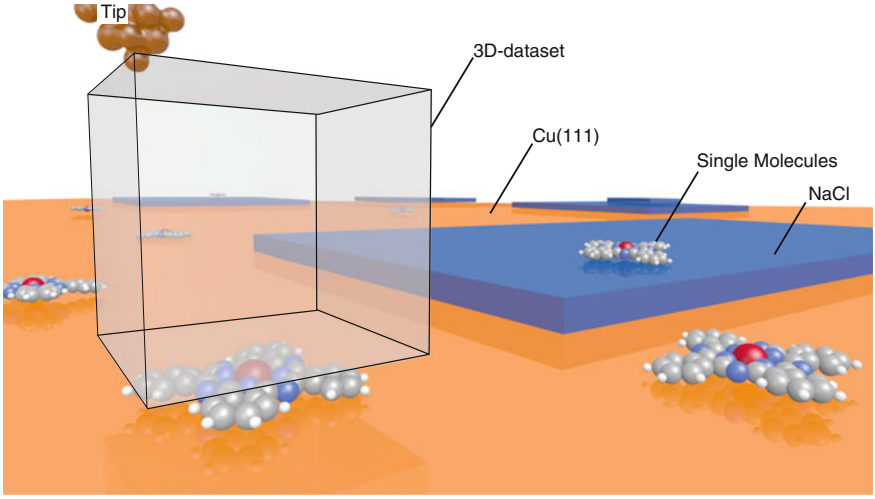

Fig. 11.1 Concept of single molecule force spectroscopy. During molecule evaporation, the substrate is kept at low temperature (below 10 K, within the microscope) to avoid any self-assembly. Insulating thin layers such as NaCl can also be grown on *top* of which molecules are deposited. 3D-spectroscopic dataset of force and current can be then conducted on such "individualized" molecules having different adsorption characteristics and thus variable intrinsic properties

keeping their electronic integrities, which are then probed by STM/nc-AFM experiments [51, 70, 71]. Such reference samples, i.e. NaCl thin films/Cu(111), is also well known for functionalizing tip apexes with various molecules adsorbed on NaCl layers to perform high-resolution imaging [55]. The cuboid of Fig. 11.1 schematizes a 3D-databox where the spectroscopic measurements are usually acquired.

11.2.2 Three-Dimensional Spectroscopic Measurements

11.2.2.1 Acquisition Method and Experimental Setup

3D-dynamic force spectroscopy measurements (3D-DFS) are able to investigate surfaces with sub-angström resolution in real space. In frequency modulation atomic force microscopy (FM-AFM or nc-AFM), the observable is the frequency shift (Δf) with respect to the resonance frequency (f_0) of an oscillator resulting from the interaction forces F between a nano tip and the surface. Using numerical conversion algorithms, 3D-fields of the site-dependent interaction forces as well as the surface potential energy landscape can be extracted above a material in the three dimensions (x, y, z) from the $\Delta f(z)$ spectra (Fig. 11.2b) [72]. Electrostatic forces can be also locally probed by measuring the tip-sample interaction with respect to the sample voltage, V, between tip and sample ($\Delta f(V)$, Fig. 11.2d). Through the measured

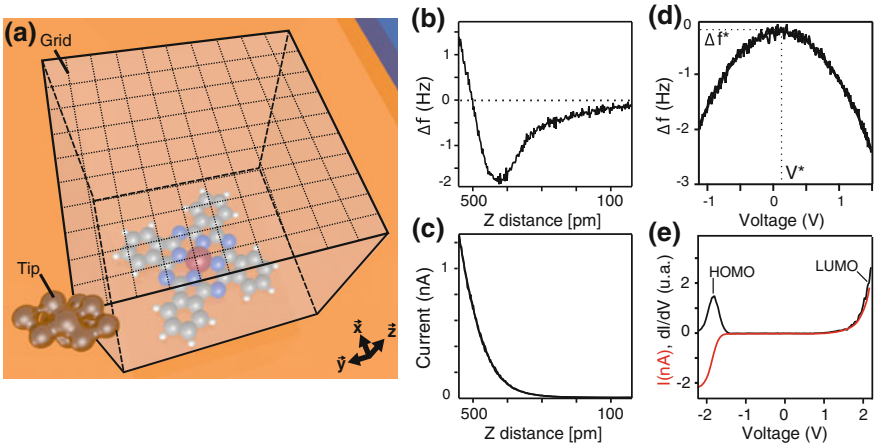

Fig. 11.2 Illustration of a 3D-spectroscopic measurements above a single molecule. The grid on *top* of the molecule set up by the experimentalist predefines the resolution of the final spectroscopic map. At every point of the grid, the variations of Δf and tunneling current I_t versus the tip-sample distance Z or the bias voltage V are recorded. Typical single spectra of $\Delta f(z)$, $I_t(z)$, $\Delta f(V)$ and $I_t(V)$ obtained at one point of the grid are plotted in (**b**), (**c**), (**d**) and (**e**) respectively. In (**e**), HOMO and LUMO refer to Highest Occupied Molecular Orbitals and Lowest Unoccupied Molecular Orbitals respectively

tunneling current I_t versus the tip-sample distance z or V (Fig. 11.2c, e), additional information of the sample conductivity can be obtained such as the electronic band gap of a material and the electronic states of single molecules.

We use a commercial low-temperature STM/AFM system from Omicron GmbH operated with Nanonis electronic from SPECS. Both STM and AFM data are acquired with a tuning fork sensor in the qPlus configuration having an external wire for the tunneling current. The W tip is usually poked into an atomically cleaned metal (Cu(111)) to sharpen and chemically define its apex. The parameters usually used for force spectroscopy are $A = 50$ pm, $k = 1800$ N/m with $Q = 15{,}000$–$60{,}000$ at 5 k and $f_0 \approx 25$ kHz. As depicted in Fig. 11.2a, we usually acquire data with the grid mode [63] meaning that single-point spectroscopies of Δf and tunneling current I_t are recorded simultaneously at each point of the predefined matrix of $x \times y \times z$ nm^3 length containing $x' \times y' \times z'$ data points. Since such force and current mapping usually takes more than 10 h, small thermal drift even existing at helium temperature measurement can induce significant measurement errors. Furthermore, this thermal drift is non-linear in the measurement time-scale. The so-called feed-forward method [37, 73] cannot be used in such cases. Thus, we developed a "drift-corrected three dimensional force and current spectroscopy", in which the tip-sample relative position is corrected between each spectroscopic curve by using atom tracked tip positioning [74]. Figure 11.2b–e shows typical single point spectra of $\Delta f(z)$, $I_t(z)$, $\Delta f(V)$ and $I_t(V)$, *dI/dV* that are used to investigate the fundamental properties of molecules at the atomic scale.

11.2.2.2 Determination of Interaction Forces and Potential

The correlation between normal tip-sample forces F_{ts} and measured Δf has been described in detail by [37–39, 47, 48, 75, 76]. The following part focuses on the essential formulas. During the approach of the oscillating qPlus sensor to the surface, the resonance frequency shifts under the action of the tip-sample interaction forces. The motion of the AFM tip can be described as a weakly perturbed harmonic oscillator [47]. In the case of qPlus sensors operating with small oscillation amplitudes (A<100 pm), the relation between frequency shift $\Delta f = f - f_0$ and the tip-sample force F_{ts} or the tip-sample stiffness k_{ts} can be approximated by:

$$\frac{\Delta f(z)}{f_0} = -\frac{1}{2k}\langle\frac{\partial F_{ts}(z)}{\partial z}\rangle \approx \frac{k_{ts}}{2k} \tag{11.1}$$

where z is the tip-sample distance, f_0 the resonance frequency, k the sensor stiffness, $\langle\partial F_{ts}(z)/\partial z\rangle$ is the averaged force gradient over the tip oscillation cycle which is considered constant for small oscillation amplitudes and thus approximated by $k_{ts} = -\partial F_{ts}(z)/\partial z$, the tip-sample stiffness.

However, k_{ts} can vary by several order of magnitudes when using larger oscillation amplitudes. A more general expression to calculate F_z from the Δf and not restricted to only small oscillation amplitudes was obtained using first-order derivation in the Hamilton-Jacobi approach and given by [47, 76]:

$$\Delta f(z) = -\frac{f_0}{\pi k A}\int_{-1}^{1} F_{ts}(z + A(1+u))\left(\frac{u}{\sqrt{1-u^2}}\right)du \tag{11.2}$$

with f_0 resonance frequency, A oscillation amplitude and k stiffness of the oscillator and F_{ts} tip-sample force interaction. In the integral, the term $u/\sqrt{1-u^2}$ acts as a weight function which help to describe the contribution of Δf with respect to the oscillation amplitude [38]. From this formula, the experimental $\Delta f(z)$ is correlated to the tip-sample interaction force by a mathematical transformation inversion. Several approximation methods have thus been proposed to simplify this inversion [17, 77, 78]. The method we employed is the analytic approximation developed by Sader and Jarvis [75] giving $F_{ts}(d)$ from the measured $\Delta f(z)$ as follows:

$$F_{ts}(d) = \frac{2k}{f_0}\int_d^{\infty}\left(1 + \frac{A^{1/2}}{8\sqrt{\pi(z-d)}} - \frac{A^{3/2}}{\sqrt{2(z-d)}}\frac{\partial}{\partial z}\right)\Delta f(z)dz, \tag{11.3}$$

A further integration gives the tip-sample surface potential $U_{ts}(d)$ as :

$$U_{ts}(d) = \frac{2k}{f_0}\int_d^{\infty}\left(z - d + \frac{A^{1/2}}{4}\sqrt{\frac{z-d}{\pi}} + \frac{A^{2/3}}{\sqrt{2(z-d)}}\right)\Delta f(z)dz \tag{11.4}$$

with d is the closest tip-sample distance, z the tip-sample distance, f_0 the resonance frequency of the oscillator, A its oscillation amplitude and k the stiffness. Even though these analytic expressions can be easily implemented to post-process the $\Delta f(z)$ curves, a particular attention must be taken when acquiring the data to obtain an high accuracy of the extracted F_{ts}. The Sader and Jarvis algorism indeed requires to know the whole $\Delta f(z)$ pathway, from the closest tip-sample distance ($z = d$) up to a distance where the oscillator is unaffected by the tip-surface interactions ($z = \infty$). Since the long-range force contributions are in principle not site-dependent, we always record one "long" $\Delta f(z)$ curve (typical sweep distance 5–10 nm) after acquiring a 3D-dataset in order to extract the long-range vdW background of each single curve [23]. Using Sader and Jarvis algorism, the $\Delta f(z)$ curves must also be free of instabilities or jumps to avoid errors in the force and potential extraction due to the integration process [38]. Finally, the intrinsic parameters of the qPlus (k, A and f_0) have to precisely estimated to avoid further offsets. From the $\Delta f(z)$ spectra taken at each point of a 2D-grid, $F_{ts}(x, y)(z)$ can be determined at every point. In this way, a force field in three dimensions, $F_{ts}(x, y, z)$, can be built up above the choosen surface [60, 61, 63, 74, 79]. A further integration of $F_{ts}(x, y, z)$ will give the tip-surface potential $U_{ts}(x, y, z)$ [32]. The derivation of this potential $U_{ts}(x, y)$ along x and y will also provide maps of the lateral forces $F_l(x, y)$ [36].

11.2.2.3 Local Contact Potential Difference (LCPD) Mapping

Kelvin Probe Force Microscopy (KPFM) is an advanced AFM technique which combines the high spatial resolution of the AFM technique and the measurement of work function introduced by Lord Kelvin [80]. When two parallel plate capacitors face each other and have different work functions ϕ_1 and ϕ_2 are electrically connected via a back electrode, electrons are transferred to align their Fermi levels. A difference of potential appears in the vacuum barrier separating the plates appears, so-called contact potential difference (CPD) and defined as: $V = (\phi_1 - \phi_2)/|e|$ with e the charge of the electron. The original method is thus based on the measurement of displacement current generated between the two plates, induced by the CPD and continuously measured.

Based on the ncAFM mode, KPFM detects the variation of electrostatic forces between tip and surface. A dc-voltage is applied to minimize the electrostatic forces between tip and sample, then defined as $V_{LCPD} = (\phi_{\text{tip}} - \phi_{\text{sample}})/|e|)$, when an ac-voltage modulation is applied to the tip to track the electrostatic force contribution. The curve has a parabola shape because it probes the electrostatic force contribution of tip-sample interactions described by in the simplest approach:

$$F_{el} = \frac{1}{2}\frac{dC}{dz}\Delta V^2 \tag{11.5}$$

where C is the capacitance of the tip-sample capacitor, $\Delta V = V_{\text{tip}} - V_{LCPD}$ is the potential difference between tip and the sample V_{LCPD}. Note that C depends on the tip-sample distance and the geometry of the probe.

An alternative of the conventional dynamic KPFM mode [80] is to determine the LCPD with spectroscopic curves by measuring the tip-sample interaction, $\Delta f(V)$, as a function of the bias voltage V. A typical $\Delta f(V)$ spectra is shown in Fig.11.2d. The LCPD is given by the position of the maximum of the parabola corresponding to the LCPD compensation, noted $V^* = V_{LCPD}$, and estimated by numerical fitting. Based on several $\Delta f(V)$ spectroscopic curves acquired over a 2D- or 3D-matrix, $LCPD(x, y)$ maps can be built-up after extraction of V^* at each position. This approach is slower than KPFM since the curve needs to be acquired over a large bias voltage variation at every point. However, the interpretation of LCPD is more straightforward since it avoids additional feedback loops which can produce crosstalk effects. In the following, we will refer to this spectroscopic technique as LCPD mapping rather than a "true" analogue of the KPFM despite of the fact they measure the same physical quantity.

LCPD mapping at low temperature has already shown the detection of different charge states [50, 52, 53] and the charge distributions within single molecules at the atomic scale [55–57]. The physical origin of these contrasts at the atomic level can be correlated to "work function changes" but further to local dipole moments, inhomogeneties of electron distributions at step edges or point defects as well as local polarization effects. It is important to differentiate the short- and long-range contributions of the electrostatic forces, one being related to bulk properties of a material (long range) and the other one from for example to adatoms or single charged point defects (short-range). Several models have been developed taking into account the short-range, long-range contributions and polarization effects when interpreting the experimental data [81–83]. Combining low temperature spectroscopic experiments with theories is most likely the key to further develop our understanding of atomic-scale measurements of electrostatic forces.

11.2.2.4 Scanning Tunneling Spectroscopy-STS

The tunneling current I_t measured by STM depends on the local density of electronic states (LDOS) close to the Fermi level of the sample. When the STM tip is brought close to the sample, the wavefunctions of tip and sample overlap. In the low bias voltage application, the variation of I_t with respect to the tip-sample distance z is monotonic and expressed as follow [84, 85]:

$$I_t(z) \propto \frac{\text{const.}V}{z}\exp^{-2\kappa z} \tag{11.6}$$

with κ is the inverse decay length. κ is written:

$$\kappa = \sqrt{\frac{2m}{\hbar^2}\frac{(\phi_{\text{tip}} + \phi_{\text{samp}})}{2} - E + \frac{eV}{2}} \tag{11.7}$$

where ϕ_{tip} and ϕ_{samp} are the work function of the tip and sample respectively. A typical experimental curve of $I_t(z)$ is shown in Fig. 11.2b. In constant-current mode, the I_t contribution is approximately the integrated LDOS of the surface. The tunneling current at a fixed (x, y) position and at constant tip-sample distance z and bias voltage V is given by:

$$I_t(V, x, y) \propto \int_0^{eV} \rho_t(E - eV)\rho_s(E, x, y)T(E, V, z)dE \tag{11.8}$$

with ρ_t and ρ_s are the DOS of tip and sample respectively, E the energy and T is a transmission function describing the probability of electrons to tunnel between tip and sample. It is well-established that the derivative of the tunneling current is proportional to the surface LDOS. Its expression is:

$$dI_t/dV \propto T(E, V, z)\rho_s(E, x, y)\rho_t(0) + \int_0^{eV} \rho_s(E, x, y)\frac{d[T(E, V, z)\rho_t(E - eV)}{deV}dE \tag{11.9}$$

At constant height and for low bias voltages, the transmission coefficient T is assumed to be energy independent. Therefore (11.7) thus links directly the derivative *dI/dV* to the LDOS of the sample at a fixed tip-sample position z. Nowadays, the study of molecular systems is widely conducted using *dI/dV* providing a accurate positioning of their filled (Highest Occupied Molecular Orbitals-HOMO) and empty electronic states (Lowest Unoccupied Molecular Orbitals-LUMO) [70]. Combining force and current spectroscopy is a powerful asset to better understand electronic properties of single molecules.

11.3 Probing Mechanical Properties at the Sub-molecular Level

11.3.1 3D-Force Field of Fullerene C_{60}

To reveal the capabilities of force spectroscopic measurements to study single molecules, we first investigated fullerenes C_{60} adsorbed on Cu(111) [60]. The chemical structure of the molecule is shown in Fig. 11.3a and consists of 12 pentagonal and 20 hexagonal carbon rings. C_{60} deposited at room temperature on the surface nucleate at step edges and form 2–3 monolayers islands, but we focused on single molecules adsorbed on top of those islands. The 3D-force field presented in Fig. 11.3 was built up from several $\Delta f(z)$ spectroscopic curves taken above the molecule in a box of $1.1 \times 1.1 \times 0.5$ nm^3 containing $60 \times 60 \times 128$ data points. The total recording time

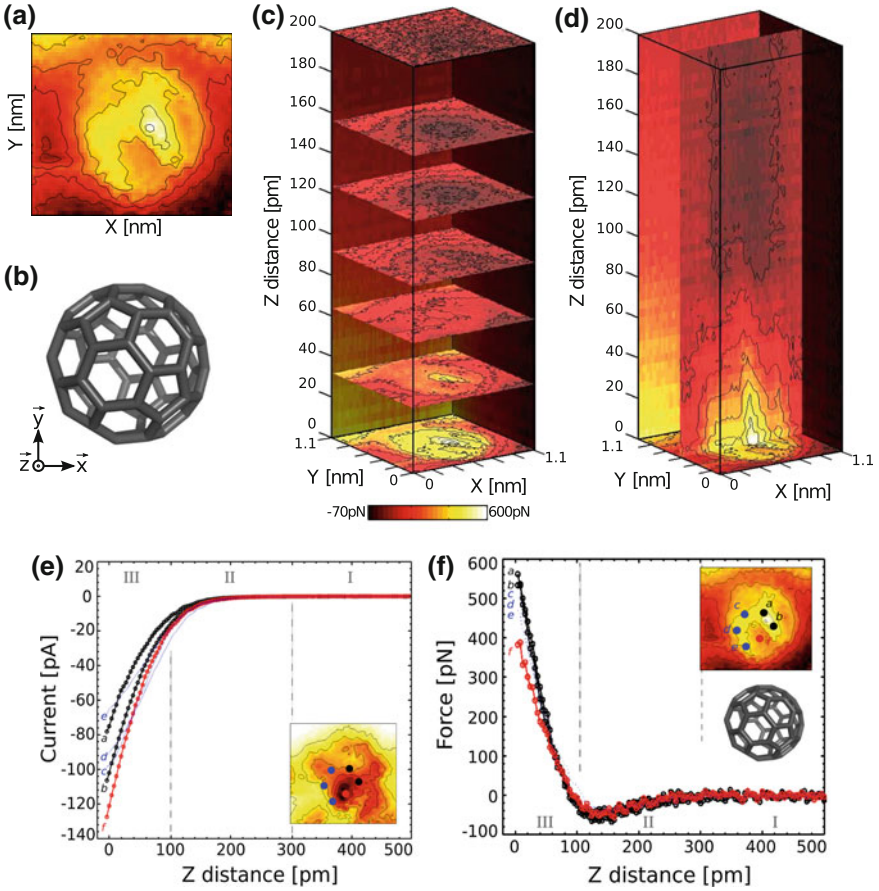

Fig. 11.3 **a** Closest constant-height $F_{ts}(x, y)$ map extracted from a 3D-force field showing intramolecular resolution. **b** Molecular orientation according to the $F_{ts}(x, y)$ map. **c** Successive $F_{ts}(x, y)$ maps at different tip-sample separations, and **d** $F_{ts}(x, z)$ cross-section taken at the center of the molecule, revealing the contrast evolution with respect to the tip-molecule distance z. The z axis is distorted for a better readability. Total 3D-DFS parameters, $1.1 \times 1.1 \times 0.5\,\text{nm}^3$ with $60 \times 60 \times 128$ data points, V $\approx 300\,\mu$V, A $= 60$ pm

was approximately 13 h and, as previously described in Sect. 11.2, we also recorded $\Delta f(z)$ of 10 nm sweep distance to estimate long-range force contributions and extract the total normal force.

Figure 11.3b shows such a $F_{ts}(x, y)$ map obtained at the closest tip-sample z whereas Fig. 11.3c, d show various plots of the 3D-force field $F_{ts}(x, y, z)$. Figure 11.3b clearly shows the chemical structure of the C_{60} with an edge between polygons on top of the molecule and thus allows an unambiguous interpretation of the molecule orientation as depicted in Fig. 11.3a. The data also confirms that intramolecular resolutions of molecules can be obtained via force spectroscopy as first

shown by Gross et al. [50]. In addition to sub-molecular resolution imaging, such results reveal that the dominant force regime in sub-molecular imaging is the Pauli repulsive force regime [50]. With qPlus sensors operated at small amplitudes, intramolecular resolutions are usually obtained by probing the Pauli repulsive regime of forces [50]. The largest repulsive forces is ≈600 pN at the top of the molecule whereas at the periphery of the structure the forces are lowered to ≈400–500 pN due to the curvature of the molecule. In contrast to CO functionalized tip experiments (see Chap. 12), the values of these repulsive forces is sensibly higher, that we assume to result from the more reactive Cu-terminated tips. Figure 11.3c, d describes successive $F_{ts}(x, y)$ constant-height maps at different tip heights and a vertical cross section $F_{ts}(x, z)$ taken at the center of the molecule, respectively. It shows that a variation of the z distance of ≈80 pm is sufficient to induce the disappearance of the structure resolution during constant-height imaging. For tip-sample separations larger than 80 pm, the contrast essentially results from short-range attractive force interactions. The molecules appear as a homogeneous protrusion similar to previous nc-AFM contrasts on insulators or semiconductors [86].

Figure 11.3e, f shows individual tunneling current and force spectroscopic curves obtained at specific (x, y) positions above the molecule (see insets Fig. 11.3f). We particularly focused our interest on the carbon sites of the buckyball structure (marked by blue and back dots) and the center of the carbon ring (red dots). In the I_t curves (Fig. 11.3e), the center of the carbon ring (red curve) has the highest value of tunnelling current (≈130 pA) whereas the different C sites appear with less intensity. In contrast, the force spectroscopic curves (Fig. 11.3f) have a different behaviour. For z distances where the tip probes short- and long-range attractive forces (region I and II), the curves coincide thus indicating site-independent information. When the z distance is smaller than 100 pm, strong differences arise induced by the contribution of site-dependent repulsive forces. We observe that the maximum extracted interaction forces above carbon atoms varies from 450–580 pN depending on the site. This variation is again the consequence of difference of the tip-sample distance z at the closest point due to molecule curvature. The red curve was obtained at the center of the carbon ring (site f in Fig. 11.3f) and exhibits the smallest interaction force at the closest point (390 pN).

Importantly, the slopes of the $F(z)$ curves in the repulsive regime (Fig. 11.3f) correspond to the local force gradient variations and can be interpreted as local elastic properties appearing between the structure of the C_{60} molecule and a Cu-terminated tip. Above carbon atoms, vertical force gradient k_{ts} vary from ≈9 to 7 N/m. At the center of the carbon ring, k_{ts} is lowered to ≈4 N/m. Since the dissipation signal was extremely small (≤10 meV/cycle), we conclude that the local deformations are purely elastic and not plastic. Therefore, these results demonstrate that mechanical properties of single molecules can be probed at the sub-molecular scale via force spectroscopic measurements. However, the interpretation of such data is a challenging task. Concluding whether the tip, the molecule structure, the substrate or the whole system is deformed is not straightforward and often require additional numerical calculations. For example, the deformation of the substrate under the probed C_{60} [66] or the distortion of CO molecules under similar experiments [87, 88] has

been already demonstrated. In the following subsections, we will thus focus on experiments showing that only mechanical properties of adsorbed molecules can be probed at the sub-molecular scale.

11.3.2 Directed Rotation of Porphyrins

In comparison to the fullerene structure which has a high mechanical stability, porphyrin molecules are expected to be more deformable since they contain many "bendable" C–C bonds between their core and the peripheral end-groups. Figure 11.4a depicts the chemical structure of the H_2TBCPP porphyrin molecule that we employed. The molecule consists of a free-base porphyrin core functionalized with two meso-(3,5-dicyanophenyl) and two meso-(3,5-di-tert-butylphenyl) peripheral rings. Carbonitrile groups (CN) are well-known to enhance organometallic complexation, which in our case ensures a strong anchoring to the Cu(111) surface. STM images (Fig. 11.4b) show individual molecules oriented along the [110] and equivalent symmetry directions of the Cu(111) surface.

The single molecules appears by STM (Figs. 11.4b, 11.5a) as two bright spots and two darker one, corresponding to the di-tert-butylphenyl and dicyanophenyl moieties, respectively. Upon adsorption particularly due to the strong CN-Cu interaction between molecule and surface, a conformational change occurs meaning that the molecular structure is strongly deformed. Instead of the C_4 symmetry of the gas phase, molecules are flat-lying and have a C_{2v} symmetry so called saddle-conformation. In this conformation, the dicyanophenyl-groups are slightly rotated out of the surface plane in such way that one CN group always remains closer towards the substrate compared to the other one. Steric hindrance between the adjacent legs further leads to a bending of the pyrrole units of the central macro-cycle up- and downwards by about 20°–30° [89].

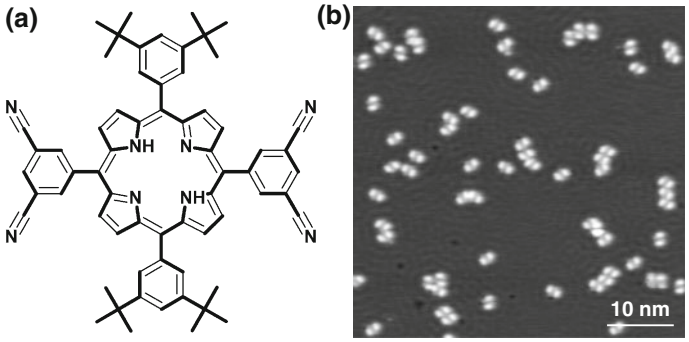

Fig. 11.4 **a** Chemical structure of the free-base porphyrin equipped with two meso-(3,5-dicyanophenyl) and two meso-(3,5-di-tert-butylphenyl) rings. **b** Constant-current STM image of single porphyrins adsorbed on Cu(111) adopting a saddle-shape geometry (I_t = 25 pA, V = 500 mV)

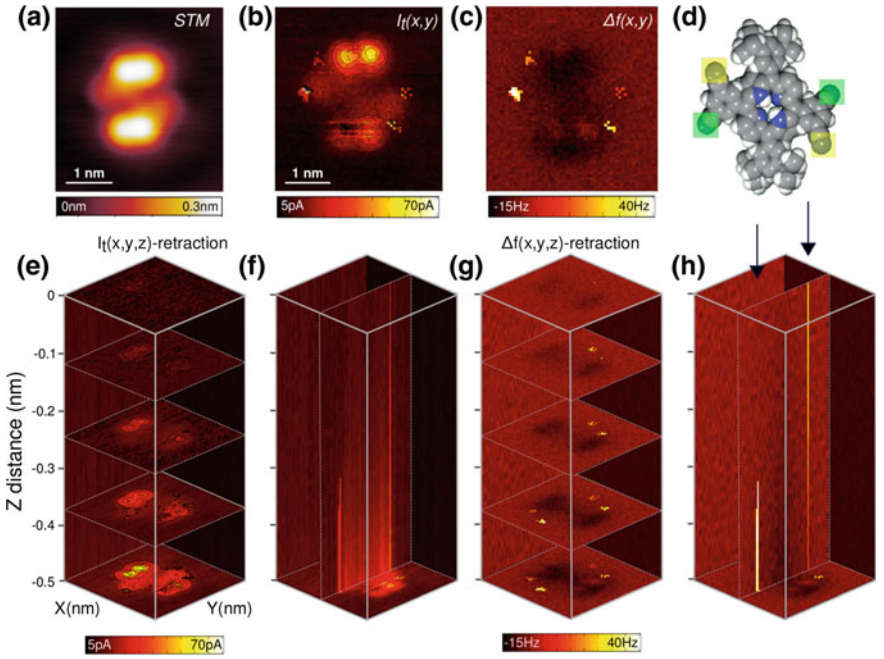

Fig. 11.5 **a–c** show a constant-current STM image, the closest $I_t(x, y)$ and $\Delta f(x, y)$ maps obtained a single porphyrin, respectively. **d** depicts the molecular adsorption symmetry. **e, f** Are $I_t(x, y)$ maps at different tip heights and a $I_t(x, z)$ crosssection, whereas (**g, h**) are the corresponding $\Delta f(x, y)$ maps and $\Delta f(x, z)$ crosssection. Four spots of positive frequency shift are identified with sub-molecular precision in the $\Delta f(x, y)$ maps (**c**) and help the chemical recognition of the N atom locations of the dicyanophenyl side groups in the molecule structure. Tip-molecule chemical bindings can be done through them allowing to apply local deformations to the molecule

11.3.2.1 Carbonitrile Group Recognition and Force-Induced Rotations

Systematic 3D spectroscopic measurements were conducted above single porphyrins in cuboids of $3.2 \times 3.2 \times 0.5$ nm^3 consisting of $68 \times 68 \times 128$ data points. The closest recorded $I_t(x, y)$ map (Fig. 11.5b) reveals the local electronic density of the molecule at the Fermi level and recalls the shape observed by STM (Fig. 11.5a). In contrast, the closest $\Delta f(x, y)$ map and the $\Delta f(x, z)$ cross-sections (Fig. 11.5g, h) show the molecule mainly as a dark protrusion all along the tip-sample z distance. Since only long-range attractive interaction forces are inducing the molecular contrast, the achievement of resolution of the chemical structure cannot be expected. A the periphery of the molecule, four localized peaks with more positive Δf ($\approx$30 Hz) corresponds to the exact location of the N atoms of the CN side groups. The same phenomena is also visible in the current channel, manifested by abrupt jumps to higher currents (Fig. 11.5e, f). The Δf remains positive several hundreds of picometers during the tip retraction (see arrows in Fig. 11.5h).

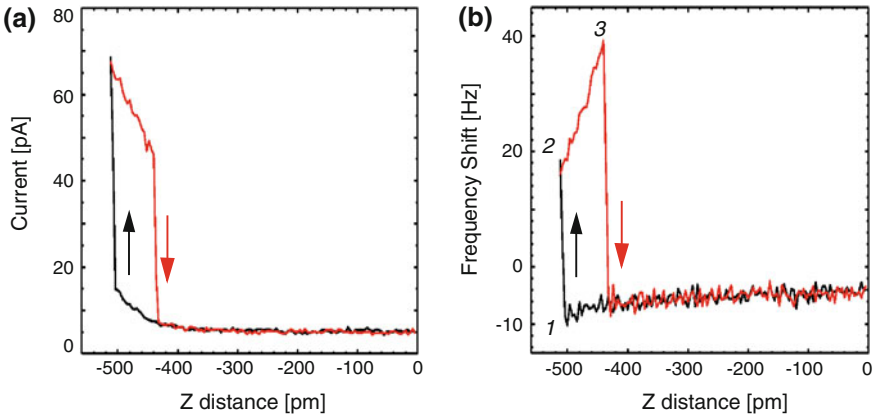

Fig. 11.6 **a** Individual approach-retract $I_t(z)$ and $\Delta f(z)$ curves taken at the N atom position. A tip-molecule junction is formed during approach (transition 1–2 in **b**) which allows the manipulation of the dicyanophenyl leg during retraction (region 2–3)

To better understand these local instabilities, we plot single approach/retract $I_t(z)$ and $\Delta f(z)$ curves recorded at a single N site. Both curves (Fig. 11.6a, b) feature a hysteresis loop close to $z = 0$ between the forward and backward sweeps with abrupt jumps in I_t and Δf, that we attribute to a junction formed between the N atom of the molecule and the Cu-terminated tip. The integration of the $\Delta f(z)$ curve along the z direction up to 1 (Fig. 11.6b) represents the tip-sample interaction force $F_{ts} \approx 180$ pN required to create the bond. The tip-sample stiffness k_{ts} extracted from the Δf is ≈ 1.5 N/m at 1 and corresponds to the stiffness of the tip-molecule junction. This chemical interaction results from the coordination between Cu adatoms of the tip apex and a single N atom of the CN group. While the tip is being retracted (region 2–3), this bond is sufficiently strong to lift the CN group vertically. At larger tip-sample distance ($z \geq 400$ pm), $I_t(z)$ and $\Delta f(z)$ perfectly coincide indicating that the hysteresis process do not induce strong tip changes. Importantly, the manipulated side group recovers its initial position which was systematically confirmed with STM images afterwards. The hysteretical switching is reversible and observed regardless of the considered molecule and the targeted N atom. Therefore, we demonstrate that force spectroscopy can be employed for recognizing specific chemical groups of a single molecules. In the following we used this ability recognize and control this bound in order to apply localized forces to the molecular structure leading to its controlled deformation.

Using this method, we found that a planar rotation of the molecule is reliably induced on the surface with a single z spectroscopic curve when the tip is slightly further approached ($\approx$20 pm) compared to Fig. 11.6. Details of the spectroscopic curves can be found in [62]. The manipulation process, depicted in Fig. 11.7a–c, consists of a 60° rotation. The rotation direction with respect to the initial orientation is mediated by the N atom chosen to generate the tip-molecule junction (Fig. 11.7a). Thereafter,

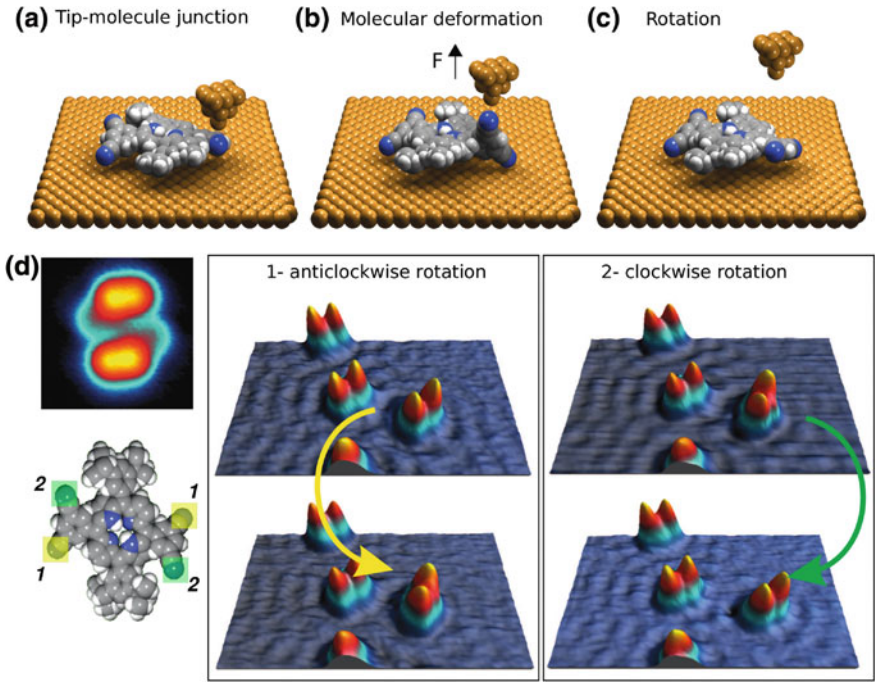

Fig. 11.7 a–c Cartoon of the manipulation experiment consisting of the rotation of the dicyanophenyl end group by the tip. **d** The molecule has four CN function which can be used for the manipulation process. Anti-clockwise and clockwise rotations are induced by taking a single spectroscopic curve at *2* and *1*, respectively

a single spectroscopic curve is acquired inducing the rotation of the dicyanophenyl side groups (Fig. 11.7b) and the distortion of the molecular structure. The manipulation of the porphyrin leg induces the displacement of the CN group in contact with the surface. By further retracting the tip, the tip-molecule junction ruptures and the molecule readopts the saddle conformation and rotates by 60° (Fig. 11.7c). We found that clockwise rotations are induced by attaching the tip to the N sites noted 2, whereas counterclockwise rotations arise from the sites 1 regardless of the chosen enantiomer (Fig. 11.7d). Furthermore, to avoid lateral shifts due to drift or piezo creep and to reach successfully to the N site, atom-tracked tip positioning was activated above one tert-butyl group before the spectroscopic curve. These results thus demonstrate the controlled vertical, lateral and rotational manipulations of isolated porphyrins by means of single force spectroscopy. It particularly opens the study of more complex molecular systems using this technique.

11.3.3 Vertical Manipulation of Long Molecular Chains

To further investigate the mechanical degree of freedom of single molecule structure, we mimicked pulling experiments of long molecular chains as performed in biology with for example proteins and DNA. For that purpose, we used a well-defined polymeric chain synthesized in-situ and measured its mechanical properties with force spectroscopy while lifting it [90].

Based on on-surface chemistry approach [91, 92], polyfluorene molecular chains were synthesized on Au(111) from evaporated dibromoterfluorene molecules (DBTF, Fig. 11.8a). The molecule consist of three fluorene units terminated by Br atoms at both ends. At elevated temperature (490 K), a debromation process occurs allowing the radicals to diffuse and covalently link as molecular chains. Previous experiments

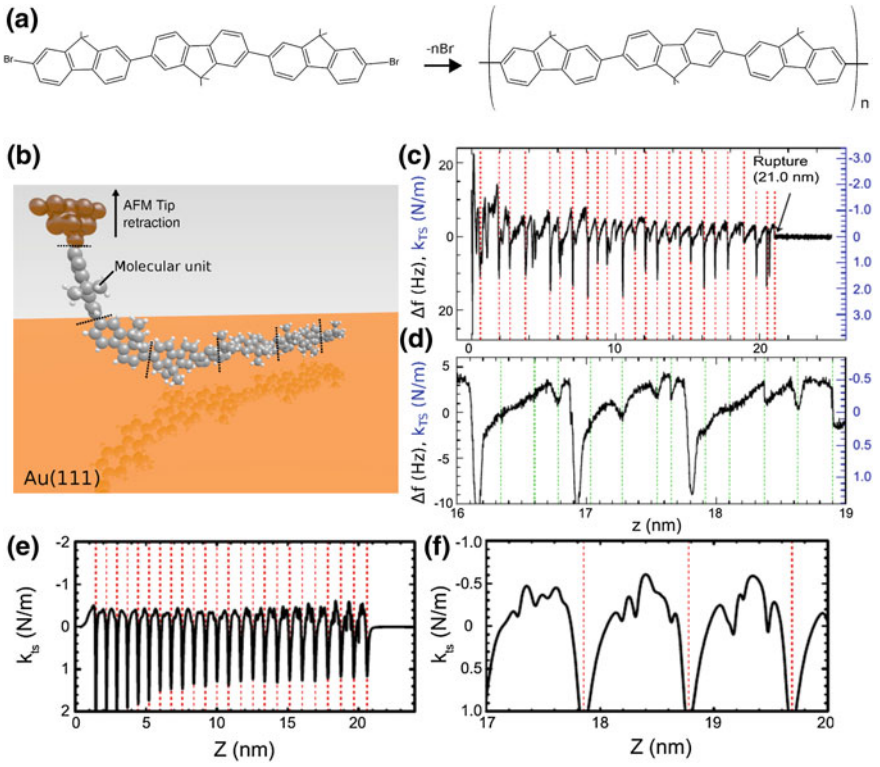

Fig. 11.8 **a** Polymerization reaction induced on Au(111) to produced long molecular chains from dibromoterfluorene (DBTF) molecules. **b** Concept of the experiment: the AFM tip connected to the end of the molecular chain is employed to performed pulling experiments. **c** $\Delta f\,(z)$ curve obtained during the lifting of the macromolecule. The detachment is marked by the *arrow*. **d** Magnification around $z = 17.5$ nm. **e** Calculated dependence of the normal force gradient versus tip-surface distance z. **f** Magnified view showing superimposed modulation between three detachment events

by Lafferentz et al. demonstrated that vertical manipulations of single chains can be further performed to measure their conductance [93]. To do that, the Au-terminated tip apex is positioned precisely at the end of the molecular chain close enough to connect to the chain.

With the same approach, pulling experiments were performed to measure the mechanical behavior of polymers during their lifting as depicted in Fig. 11.8b [90]. Figure 11.8c shows the measured $\Delta f(z)$ curve up to a distance of 25 nm during the vertical manipulation of a 20-nm long chain. The effective stiffness, calculated from the Δf, is indicated on the right scale. A periodic variation is observed, with each period terminated by an abrupt jump (indicated by the red broken lines). The number of periods (24) exactly corresponds to the number of the fluorene units previously observed by STM imaging. At the end of the $\Delta f(z)$ curve, the Δf is $\approx$0 Hz as a result of the detachment of the molecular wire from the surface. Interestingly, the periodicity of the curve is $\approx 0.91 \pm 0.07$ nm which coincides with the length of a single fluorene unit of the chain (0.845 nm). We conclude that the chain has a stepwise detachment from the surface, unit after unit, which is readily detected by force spectroscopy. A closer observation of few periodic events (Fig. 11.8c) also reveals that a second minor modulation marked by green broken lines. Its periodicity is close to the substrate lattice direction along which the molecular chain is sliding while being pulled (0.5 nm).

To quantify further the experimental results and explain these periodic modulations, we developed an extended version of the Frenkel-Kantorova (FK) model. In analogy to the FK model, the molecular chain is approximated by a series of coupled particles connected by equivalent springs of stiffness k and equilibrium length b. Each unit interacts with the substrate through a sinusoidal potential simulating the Au(111) surface. In addition to the FK model, a more realistic interaction potential to estimate the surface-molecule interactions was used, introduced to describe gas-atom solid interactions by Steele [94]. More details about the model can be found in [90]. As shown in Fig. 11.8e, f, the model perfectly reproduces the experimental $\Delta f(z)$ curves revealing that both periodicities resulting from the stepwise detachment as well as the sliding of each unit on the surface. It is however essential that the effective stiffness of the pulled-off segment is large compared to tip-sample stiffness ($\approx$tip-molecule bond).

A remarkable advantage of these simulations is to analytically estimate the normal force required to detach one unit (attractive force of $\approx$0.25 nN) and shows that this force is nearly independent of the length of the chain and the unit position in the chain. In addition, the model provides new insights into normal and lateral forces acting on the pulling tip which are difficult to determine from the measured Δf and energy dissipation without questionable assumptions. This simulation is remarkably simple and its flexibility further allows to adapt it to more complex molecular systems by varying interaction and deformation potentials for different units and/or adjusting parameters to account for specific interactions with atomic lattices. These results confirmed the capability of force spectroscopic experiments to probe mechanical behavior of molecular structure at the sub-molecular level. It further gives new insights into the friction phenomena during manipulation processes.

11.3.4 Lateral Manipulation of Single Porphyrin: Atomic-Scale Friction Pattern

In the following experiment, we particularly studied this sliding characteristic. Instead of pulling a molecule with the tip apex, we manipulated a single molecule laterally attached to the tip apex over an atomically clean surface [95]. To perform these lateral manipulations with single porphyrins, we intentionally terminated the tip apex with a single molecule. The molecule we used is described in Sect. 11.2 Fig. 11.4. The tip apex is decorated by picking up the molecule from the Cu(111) surface via indenting the tip onto the center of the molecule.

The friction experiments are then conducted by approaching the porphyrin-terminated tip to the Cu surface while oscillating the tuning fork sensor with small oscillation amplitudes (≈50 pm). Figure 11.9b shows a typical $\Delta f(x, y)$ map obtained by scanning the Cu(111) surface at constant height. An atomic-scale contrast is clearly observed which resembles the frictional patterns obtained by conventional Friction Force Microscopy on Cu(111). The hexagonal structure has a periodicity of ≈0.26 nm which closed to the expected one for the Cu(111) lattice of ≈0.29 nm. A dark depression is also observed in the bottom right part of the image which corresponds to a Cu vacancy of the surface. Figure 11.9c shows line profile taken within the image of the tip-sample stiffness $k_{ts}(x)$ extracted from the Δf data. The maximum k_{ts} is about 3 N/m and the average stiffness variation Δk_{ts} is ≈5 N/m which corresponds to the tip-surface stiffness mediated by the porphyrin molecule.

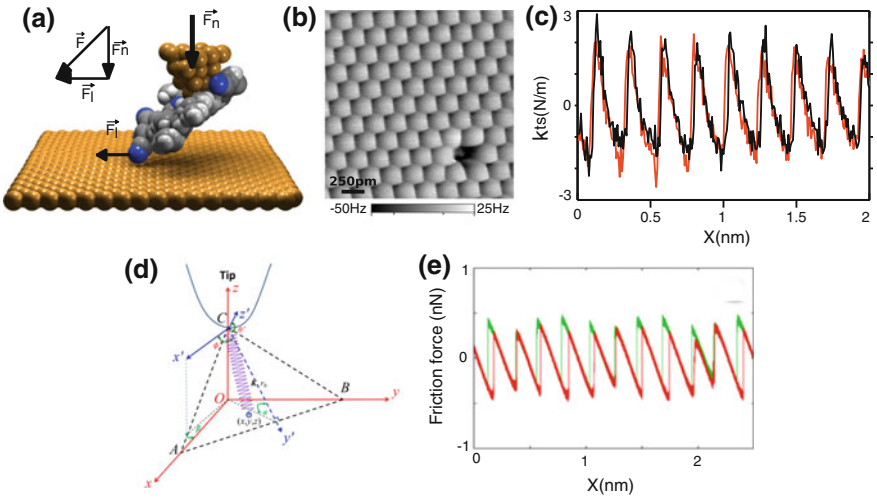

Fig. 11.9 **a** Cartoon of the experiment: a single porphyrin is attached to the tip by vertical manipulation and dragged over a Cu(111) surface. **b** Constant-height $\Delta f(x, y)$ map above the Cu(111) surface revealing a typical friction-like pattern. **c** Profile showing the sawtooth modulation. **d** Model of the simulation based on the generalized Tomlinson model and **e** the simulated profile

We attribute this to the CN end-groups and their ability to coordinate with copper atoms of both the tip and the surface (Cu-coordinated bonds) which ensure the stability of the junction and particularly its atomic nature. Moreover, we assume that the degree of freedom of the dicyanophenyl leg and particularly its σ bond attaching the leg to the porphyrin core ensures the frictional process.

In order to demonstrate this effect on friction and adhesion, we employed a generalization of the Tomlinson model using the Steele potential, that includes the reorientation of the dicyanophenyl ring with respect to the porphyrin core and stretching of the bond. As shown in Fig. 11.9d, the CN-Cu interaction is approximated by a masse m attached to the tip by a spring k. The reorientation of the porphyrin leg with respect to the porphyrin core is described by the polar angles, ϕ' and θ', of this spring as shown in Fig. 11.9d. The stretching of the bond is given by the deviation of the bond length, r' compared to the equilibrium value r_0. All these parameters can change during the simulation which are describe in details in [95].

Figure 11.9e shows the simulation of friction response for a specific scan angle which reproduces the experimental data. Different orientations of the molecule with respect to the tip were also analyzed as well scan angle [95]. As main conclusions, we emphasis that: (1) the friction loop between the forward and backward scans is small showing that, despite of the complex molecular structure attached to the tip, an atomic-scale patterns can be obtained; (2) the friction forces depend on the attachment of the molecule to the tip that is characterized by the angles; (3) forward and backward force traces can exhibit anisotropy that arises from changes of molecule conformation during sliding. Both experiments and simulations thus show that including the dynamics of degrees of freedom of molecules is crucial for understanding mechanism during their lateral and normal manipulations. Understanding such mechanical behavior might help to foresee the appropriate chemical groups with respect to surfaces as well as the preferential displacement of molecular nanomachines in motion.

11.4 Prospects in Probing the Electronic Properties of Single Molecules

With the advent of force spectroscopy at low temperature, it is now possible to investigate local contact potential difference (LCPD) between tip and sample (see Sect. 11.2) which is related to work function changes, local dipole moments, inhomogeneties of charge distributions as well as local polarization effects down to the nanometer scale. Based on the detection of electrostatic forces via $\Delta f(V)$ spectra, LCPD mapping provides insights into charges states at the atomic scale [51–54] or the sub-molecular charge distribution of single molecules [55–58]. The following examples report LCPD maps of the charge distribution of single molecules as well as an experimental approach to investigate their optical properties in the future.

11.4.1 LCPD Mapping of a Donor-Acceptor Molecule

To confirm the ability of LCPD mapping to spatially resolve charge distribution at the sub-molecular scale, we employed donor-acceptor molecules, the 4-(4-(2,3,4,5,6-pentafluorophenylethynyl)-2,3,5,6-tetrafluorophenylethynyl)-phenylethynylbenzene (FFPB), deposited at room temperature on reconstructed (2×1)-Au(110) [57]. As revealed by the STM investigation (Fig. 11.10), chains are spontaneously formed and oriented with respect to the surface orientation. The FFPB consists of four benzene rings interlinked by ethynylene units. Two aromatic benzene rings are substituted with fluorine where the two other are free-based (H-terminated). According to DFT calculation, the electronegativity of the F atoms compared to the H atoms induces a net dipolar moment of 4.27 D along the chain. The electronegativity of the F-substituted benzene rings in FFPB acts as an acceptor compared to the benzene ring of the molecule end, the being donor part. The self-assembly depicted in Fig. 11.10b is mediated by the formation of (C–F...H–C) hydrogen bonds between the fluorine units and H-terminated carbon rings, leading to the structural deformation of the molecular structure which has been confirmed by AFM imaging and DFT calculations [57].

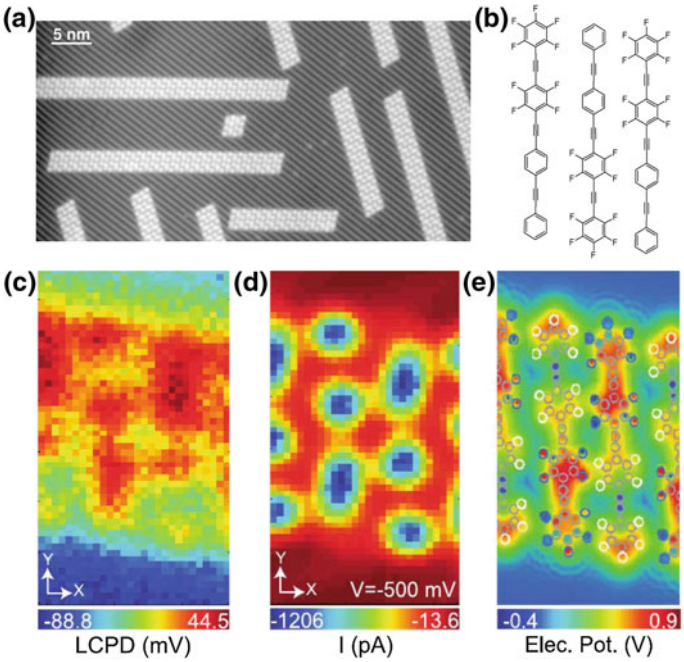

Fig. 11.10 **a** STM image of the FFPB molecules deposited on (2 × 2-Au(110)) at room temperature. **b** The chemical structure of the FFPB molecules and the self-assembly developed on Au(110). **c, d** Constant-height $LCPD(x, y, V^*)$ and $I_t(x, y, V^*)$ maps of a chain revealing intra-molecular resolutions. **e** Electrostatic potential simulated by DFT on a plane above the molecular plane

Figure 11.10c, d shows constant-height $LCPD(x, y, V^*)$ and $I_t(x, y, V^*)$ maps, respectively. The current map shows a similar contrast to the STM data with adjacent molecules in the chain having identical contrast with an opposite direction. In addition, the LCPD map reveals the internal charge distribution of the molecule. The variation of LCPD between the surface and the molecule is about $\Delta LCPD \approx 120$ mV whereas the internal charge distribution shows a $\Delta LCPD \approx 10$ mV. Since the bias voltage is applied to the tip, the negatively charged part has a more positive LCPD value. Therefore, the LCPD map allows a clear identification of the donor-acceptor parts within the molecule as further confirmed by numerical of the electrostatic potential of the system (Fig. 11.10e). With the prospects of studying photo-induced electronic effects in such molecules, LCPD mapping has thus the great advantage to precisely resolve the charge distribution of molecules down to the sub-molecular scale.

11.4.2 LCPD Mapping of Metal-Phtalocyanin on Thin Insulating Films

To preserve the electronic integrity of single molecules and thus their optical properties, it is essential to perform such experiments on insulating layers to avoid "quenching" by the metal. Therefore, we performed similar experiments on Cu-based phtalocyanin (CuPc) (Fig. 11.11a) adsorbed on two NaCl monolayers on Cu(111) [96]. STM images of the single CuPc molecule is shown in the top of Fig. 11.11b. Two molecular resonances derived from respective orbitals are clearly visible and can be attributed to the HOMO (≈2.3 V) and the LUMO (≈1.4 V). STS spectrum (blue curve) recorded at the center of the molecule confirms the positions of the HOMO and LUMO respectively (Fig. 11.11b). Importantly, this suggests that the electronic structure of the molecule is preserved upon adsorption [70]. Furthermore, a STM image acquire within the molecular band gap shows a contrast dominated by the charge distribution close to the Fermi-level, which also features a charge depletion area at the center of the molecule.

Constant-height $I_t(x, y, V^*)/LCPD(x, y, V^*)$ mapping are shown in Fig. 11.11b, c, respectively. Figure 11.11b clearly recalls the constant-current STM obtained in the band gap (Fig. 11.11b). The contrast above the molecule in the LCPD map is shifted to larger LCPD values compared to the substrate with an overall value of ≈80 mV. In addition, a modulation of the LCPD within the molecule is observed of ≈60 mV with a pronounced dip above the central Cu atom. The peripheral rings of the molecule appear with more positive LCPD (≈80 mV). In analogy with the $I_t(x, y)$ maps, the LCPD variation at the center of the molecule most likely reflects the charge depletion at the central Cu atoms of the molecule.

The recent LCPD resolutions of single molecules thus demonstrate that precise determination of the charge distributions of molecules is possible at the sub-molecular scale [55–57]. These results show that force spectroscopy might be able

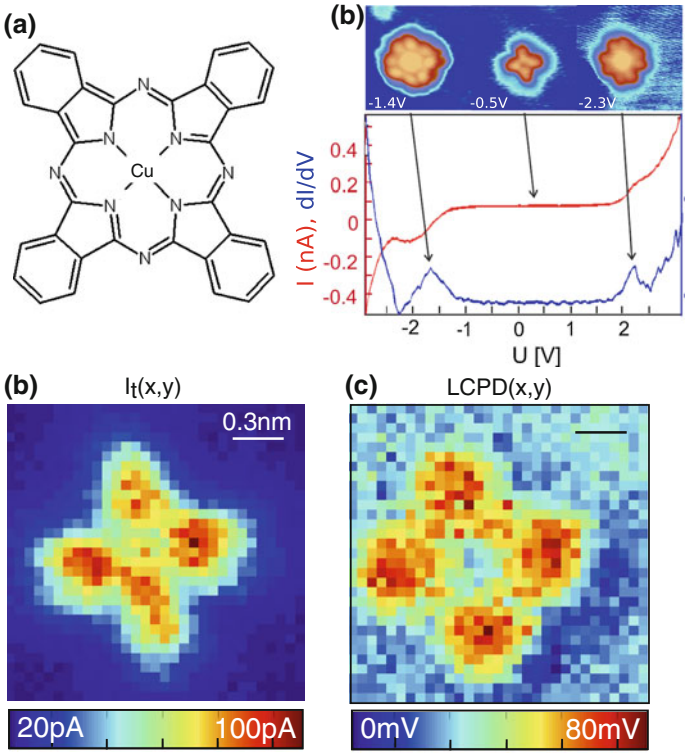

Fig. 11.11 **a** The Cu-phtalocyanin structure. **b** STS spectra and corresponding STM images of the molecule adsorbed on NaCl thin films/Cu(111). **c** Constant-height $I_t(x, y, V^*)$ maps and $LCPD(x, y, V^*)$ maps of the molecule

to detect charge transfer through single molecules via external excitation, for instance molecules contacted between nanoelectrodes or photo-excited. The following experiment describes the experimental approach we employed to detect photo-excited color centers in nanoparticles.

11.4.3 Towards Probing Optical Properties of Single Molecules

Nanodiamonds (NDs) are carbon particles with sizes from two to few tens of nanometers having a diamond structure, that we deposited on graphite in order to probe their structural and optical properties via force spectroscopy. The NDs, characterized by STM in Fig. 11.12b, also contain sub-surface nitrogen-vacancy centers (NV) which are lattice point defects of a crystal inducing new optical absorption bands. These nitrogen centers in diamond consists of a substitutional nitrogen atom associated with a vacancy in the carbon lattice (see inset Fig. 11.12a). They induce additional

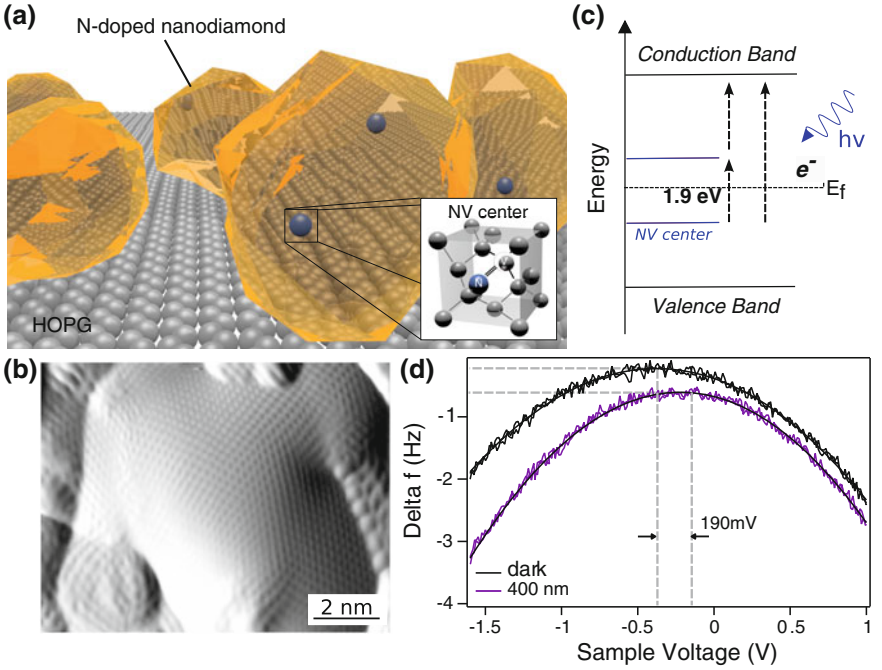

Fig. 11.12 **a** Cartoon of the experiment: nanodiamonds (ND) which contain Nitrogen-Vacancy centers (NV) are deposited on a graphite surface. **b** These *color* centers induce electronic states within the diamond band gap. **c** STM image of a single ND particle. **d** Comparison of single $\Delta f(V)$ spectra obtained above a ND under dark and 400 nm illuminations revealing a clear shift ($\approx$190 mV) of the LCPD

electronic states in the large band gap of diamond (Fig. 11.12c) and have a maximum adsorption at $\lambda = 638$ nm, so-called the zero-phonon line (ZPL). Because these particles are small, probing their optical properties is extremely challenging with conventional optical techniques. We thus conducted force and current spectroscopic measurements at low temperature to address this issue [64].

Figure 11.12d shows a comparison of $\Delta f(z, V)$ curves above the same ND under dark and 400 nm illumination. The extracted LCPD shows a variation of $V_{LCPD} = V^*$ of $\approx$190 mV. Such lateral shift of the parabola maximum is known to result from localized charges in the vicinity of the surface [51]. The vertical shift is related to the stronger electrostatic force contribution most likely arising from these charges. These observations are consistent with the photoexcitation of the defect centers of NDs and thus confirm that optical properties of materials can be measured locally. However, the variation of the force field under illumination might also induce a change of the tip-sample distance reflected then in the LCPD measurements. To ensure the interpretation, the z dependency of the LCPD must thus be know from the long-range to the short-range regime of electrostatic forces.

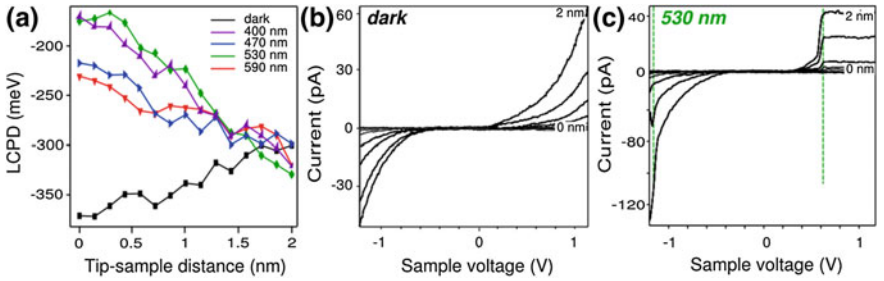

Fig. 11.13 **a** LCPD values as a function of the tipsample distance z above a single diamond under different illumination conditions. In the graph, *colors* correspond to the wavelengths (*purple* 400 nm, *blue* 470 nm, *green* 530 nm, and *red* 590 nm. **b**, **c** $I(V, z)$ spectra at different heights in dark and $\lambda = 530$ nm illumination, the z variation between curves is 15 pm

To do that, we conducted systematic $I_t(z, V)/\Delta f(z, V)$ spectroscopic measurements under five illumination conditions (dark, 400, 470, 530, and 590 nm) above the same diamond (Fig. 11.13a). In dark (dark curve) and at large tip-sample separation (z = 2 nm), the extracted LCPD value is ≈300 mV. When entering the short-range regime of electrostatic forces by decreasing the tipsample distance, the LCPD then decreases to 350 mV as a consequence of the appearance of charge images at the tip apex. At close distance (z = 0 nm), the difference of the LCPD values, $\Delta(V_{LCPD})$, observed between $\lambda = 400$ and 470 nm is ≈50 ± 5 mV and arises from different photoionization processes, i.e. electrons excited from various electronic states are transferred to the conduction band.

When illuminating at $\lambda = 590$ and 530 nm (red and green curves), a positive variation of the LCPD values is also observed which contrasts with the variation in dark. Here, the LCPD variation is induced by the continuous photoexcitation of electrons through the NV electronic states. The photocharges are only localized at the NV centers and not transferred to the conduction band due to lack of photon energy. They are however detected as LCPD variation toward more positive values. The $\Delta LCPD$ between these wavelengths at z = 0 nm is ≈70 ± 5 mV. The maximum of electronic transition for NVs is obtained for $\lambda = 530$ nm which is also the maximum LCPD shift compare to the reference value obtained in dark (190 ± 5 mV). Therefore, we conclude that the comparison of LCPD spectroscopic measurements under continuous illumination conditions is sensitive to photo-created charges in defect centers. To further confirm this claim, we also analysed the simultaneously recorded tunneling current. Figure 11.13c, d shows the evolution of the conductance curves versus the tipsample separation z under dark and $\lambda = 530$ nm illumination, respectively. A comparison of these curves clearly reveals the appearance of steps for the irradiated ND (Fig. 11.13c, green dashed lines) whereas, in dark, they are not present. These kinks in the $I(V)$ curve are the signature of the electronic states of the photo-excited NV centers. The HOMO of the NV centers lies at ≈1.2 eV below the Fermi level whereas the LUMO is found at ≈0.6 eV. The HOMO-LUMO gap is 1.8

eV and coincides with the zero phonon line of the centers obtained experimentally (1.945 eV) or theoretically predicted (1.75–1.85 eV).

Our results demonstrate that combined current and force spectroscopic measurements under continuous illumination can detect at the nanometer scale subsurface color centers of NDs through their optical excitation. We show that the z variation of the short-range electrostatic forces obtained from LCPD spectroscopy also depends on the utilized wavelenghts to photo-excite the system. Similar light-assisted spectroscopic experiments on molecular systems adsorbed on thin insulating layers might thus resolve the effect of radiation on single molecules at the sub-molecular scale.

11.5 Conclusion and Perspectives

With the advent of qPlus sensors operated at low temperature, tunneling current and force spectroscopic measurements are widely employed to reveal atomic-scale physical phenomena at surfaces. In this chapter, we reviewed our recent works applying such spectroscopic techniques to single molecules in order to reveal their intrinsic properties at the atomic scale. Particularly, the extraction of forces from the measured frequency shift helps to probe the structure of single molecules as well as their local mechanical behavior. Although the interpretation of the Δf data must be done with careful experimental considerations, appropriate numerical models provide insights into the degree of freedom of single molecules. We showed that the degree of freedom and the frictional properties of single molecular species during vertical or lateral manipulations can be understood from force spectroscopic data obtained at the sub-molecular level. We foresee that further "mechanical" based phenomena might be elucidated at this level with these techniques such as mechano-chemistry reaction or the mechanical and frictional behavior of molecular nanomachines.

In addition to their mechanical properties, we show that current/force based spectroscopic measurements help studying the electronic character of single molecules. When current information versus the tip-sample voltage V provides molecular band gaps and orbitals, our results also prove that short-range electrostatic force variations obtained from the variation of Δf as a function of V can also image the charge distribution of molecules at the sub-molecular scale. We further demonstrated that spectroscopic measurements under illumination reveal the photo-activity of defect centers in nanoparticles from the creation of localized charges. Although some experimental and theoretical issues must be still addressed, these experiments clearly open the way to study charge transfers through single molecules via external electrodes or their photo-activity under variable illumination conditions at the atomic scale.

Acknowledgments The authors are very grateful to their colleagues: Dr. Sweetlana Fremy for her help on performing the porphyrin experiments and her work on LCPD mapping of CuPc and Dr. Ali Sadeghi and Dr. Alexis Baratoff for fruitful discussions and their precious theoretical contributions. The authors also wish to acknowledge their collaborators: Pr. E. Gnecco for the extended Frenkel-Kantorova model, the group of Pr. F. Diederich for providing the porphyrin molecules, the group of Pr. L. Grill and Pr. S. Hecht for their contribution in the DBTF molecule experiments, the group of

Pr. A. Orita for providing the FFPB molecules, the group of Pr. Urback for the numerical calculations of the friction experiment with porphyrins and the group of Pr. D. Spitzer and Dr. V. Pichot for the preparation of the nanodiamond samples.
These works is supported by the from the Swiss National Science Foundation (NSF), the Swiss nanoscience Institute (SNI), the Swiss National Center of Competence in Research on Nanoscale Science (NCCR-NANO), the PRESTO project of the Japan Science and Technology agency (JST), the Polish-Swiss Project PSPB-085/2010 and the EU Cost action MP13V3.

References

1. G. Binnig, H. Roher, Ch. Gerber, E. Weibel, Phys. Rev. Lett. **49**, 57 (1982)
2. G. Binnig, C.F. Quate, Ch. Gerber, Phys. Rev. Lett. **56**, 930 (1986)
3. S. Morita, R. Wiesendanger, E. Meyer, *Noncontact Atomic Force Microscopy* (Springer, Berlin, 2002)
4. E. Meyer, H.J. Hug, R. Bennewitz, *Scanning Probe Microscopy: The Lab on a Tip* (Springer, Berlin, 2003)
5. K.C. Neuman, A. Nagy, Nature Methods **5**, 491–505 (2008)
6. F.J. Giessibl, Science **267**, 68 (1995)
7. S. Kitamura, M. Iwatsuki, JJAP **34**, L145–L148 (1995)
8. H. Ueyama, M. Ohta, Y. Sugawara, S. Morita, Jpn. J. Appl. Phys. **34**, L1086 (1995)
9. S. Orisaka, T. Minobe, T. Uchihashi, Y. Sugawara, S. Morita, Appl. Surf. Sci. **140**, 243 (1999)
10. Ch. Loppacher, M. Bammerlin, M. Guggisberg, S. Schär, R. Bennewitz, A. Baratoff et al., Phys. Rev. B **62**, 16944 (1999)
11. S.I. Kitamura, M. Iwatsuki, Jpn. J. Appl. Phys. **34**, L145 (1995)
12. A. Schwarz, W. Allers, U.D. Schwarz, R. Wiesendanger, Phys. Rev. B **61**, 2837 (2000)
13. M. Bammelin et al., Probe Microsc. **1**, 3 (1997)
14. W. Allers, A. Schwarz, U.D. Schwarz, R. Wiesendanger, Europhys. Lett. **48**, 276 (1999)
15. C. Barth, M. Reichling, Nature **414**, 54 (2001)
16. B. Gotsmann, D. Krüger, H. Fuchs, Europhys. Lett. **239**, 153 (1997)
17. B. Gotsmann, B. Anczykowski, C. Seidel, H. Fuchs, Appl. Surf. Sci. **140**, 314 (1999)
18. B. Gotsmann, C. Seidel, B. Anczykowski, H. Fuchs, Phys. Rev. B **60**, 11051 (1999)
19. H. Hölscher, W. Allers, A. Schwarz, U.D. Schwarz, R. Wiesendanger, Phys. Rev. Lett. **83**(23), 4780 (2003)
20. H. Hölscher, A. Schwarz, W. Allers, U.D. Schwarz, R. Wiesendanger, Phys. Rev. B **61**, 12678 (2000)
21. H. Hölscher, B. Gotsmann, W. Allers, U.D. Schwarz, H. Fuchs, R. Wiesendanger, Phys. Rev. B **64**, 075402 (2001)
22. H. H ölscher, S.M. Langkat, A. Schwarz, R. Wiesendanger, Appl. Phys. Lett. **81**, 4428 (2002)
23. M.A. Lantz, H.J. Hug, R. Hoffmann, P.J.A. van Schendel, P. Kappenberger, S. Martin et al., Science **291**, 2580 (2001)
24. M. Heyde, G.H. Simon, H.P. Rust, H.-J. Freund, Appl. Phys. Lett. **89**, 263107 (2006)
25. Y. Sugimoto, P. Pou, M. Abe, P. Jelinek, R. Perez, S. Morita, Nature **446**, 64 (2007)
26. J. Welker, A.J. Weymouth, F. Giessibl, ACS Nano **7**, 7377 (2013)
27. Y. Sugimoto, M. Abe, S. Hirayama, N. Oyabu, O. Custance, S. Morita, Nat. Mat. **4**, 156 (2005)
28. Y. Sugimoto, P. Pou, O. Custance, P. Jelinek, M. Abe, R. Perez et al., Science **322**, 413 (2008)
29. S. Kawai, A.S. Foster, F.F. Canova, H. Onodera, S.-I. Kitamura, E. Meyer, Nat. Commun. **5**, 4403 (2014)
30. K. Ruschmeier, A. Schirmeisen, R. Hoffmann, Phys. Rev. Lett. **101**, 156102 (2008)
31. A. Schrimeisen, D. Weiner, H. Fuchs, Phys. Rev. Lett. **97**, 136101 (2006)
32. B.J. Albers, T.C. Schwendemann, M.Z. Baykara, N. Pilet, M. Liebmann, E.I. Altman et al., Nat. Nanotechnol. **4**, 307 (2009)

33. M. Ashino, D. Obergfell, M. Haluska, S. Yang, A.N. Khlobystov, S. Roth et al., Nat. Nanotechnol. **3**, 337 (2008)
34. S. Kawai, Th Glatzel, S. Koch, A. Baratoff, E. Meyer, Phys. Rev. B **83**, 035421 (2011)
35. B. Such, T. Glatzel, S. Kawai, S. Koch, E. Meyer, J. Vac. Sci. Technol. **B 28**, C4B1 (2010)
36. M. Ternes, C.P. Lutz, C.F. Hirjibehedin, F.J. Giessibl, A.J. Heinrich, Science **319**, 1066–1069 (2008)
37. M. Abe, K. Morita, *Noncontact Atomic Force Microscopy, vol. 2* (Springer, Berlin, 2009), Chap. 2, pp. 15–30
38. O. Custance, N. Oyabu, Y. Sugimoto, *Noncontact Atomic Force Microscopy, vol. 2* (Springer, Berlin, 2009), Chap. 3, pp. 31–68
39. A. Schirmeisen, H. Hölscher, U. Schwarz, *Noncontact Atomic Force Microscopy, vol. 2* (Springer, Berlin, 2009), Chap. 5, pp. 95–119
40. R.J. Wilson, G. Meijer, D.S. Bethune, R.D. Johnson, D.D. Chambliss, M.S. de Vries et al., Nature **348**, 621–622 (1990)
41. B. Gotsmann, C. Schmidt, C. Seidel, H. Fuchs, Eur. Phys. J. B. **4**, 267 (1998)
42. A. Sasahara, H. Onishi, *Noncontact Atomic Force Microscopy* (Springer, Berlin, 2002), Chap. 13, pp. 215–232
43. Y. Sugawara, *Noncontact Atomic Force Microscopy* (Springer, Berlin, 2002), Chap. 11, pp. 183–192
44. L. Nony, E. Gnecco, A. Baratoff, A. Alkauskas, R. Bennewitz, O. Pfeiffer et al., Nano Lett. **4**, 2185 (2004)
45. Ch. Loppacher, M. Guggisberg, O. Pfeiffer, E. Meyer, M. Bammerlin, R. Lüthi et al., Phys. Rev. Lett. **90**, 066107 (2003)
46. M. Ashino, A. Schwarz, T. Behnke, R. Wiesendanger, Phys. Rev. Lett. **93**, 136101 (2004)
47. F.J. Giessibl, *Noncontact Atomic Force Microscopy* (Springer, Berlin, 2002), Chap. 6, pp. 121–142
48. F.J. Giessibl, Rev. Mod. Phys. **75**, 949 (2003)
49. M. Heyde, M. Kulawik, H.P. Rust, H.J. Freund, Rev. Sci. Instrum. **75**, 2446 (2004)
50. L. Gross, F. Mohn, P. Liljeroth, J. Repp, F.J. Giessibl, G. Meyer, Science **324**, 1428 (2009)
51. L. Gross, F. Mohn, N. Moll, P. Liljeroth, G. Meyer, Science **325**, 1110 (2009)
52. T. König, G.H. Simon, H.-P. Rust, G. Pacchioni, M. Heyde, H.-J. Freund, JACS **131**, 17544 (2009)
53. T. Leoni, O. Guillermet, H. Walch, V. Langlais, A. Scheuermann, J. Bonvoisin et al., Phys. Rev. Lett. **106**, 216103 (2011)
54. H. Walch, T. Leoni, O. Guillermet, V. Langlais, A. Scheueurmann J. Bonvoisin, S. Gauthier, Phys. Rev. B **86**, 075423 (2012)
55. F. Mohn, L. Gross, N. Moll, G. Meyer, Nat. Nanotechnol. **7**, 227 (2012)
56. B. Schuller, S.-X. Liu, Y. Geng, S. Descurtins, G. Meyer, L. Gross, Nanolett. **14**, 3342–3342 (2014)
57. S. Kawai, A. Sadeghi, X. Feng, P. Lifen, R. Pawlak, T. Glatzel, E. Meyer et al., ACS Nano **7**, 9098 (2013)
58. F. Mohn, B. Schuller, L. Gross, G. Meyer, Appl. Phys. Lett. **102**, 073109 (2013)
59. F. Mohn, L. Gross, G. Meyer, Appl. Phys. Lett. **99**, 053106 (2011)
60. R. Pawlak, S. Kawai, S. Fremy, T. Glatzel, E. Meyer, ACS Nano **5**, 6349 (2011)
61. R. Pawlak, S. Kawai, S. Fremy, T. Glatzel, E. Meyer, J. Phys. Cond. Matter **24**, 084005 (2012)
62. R. Pawlak, S. Fremy, S. Kawai, T. Glatzel, H. Fang, L.-A. Fendt et al., ACS Nano **6**, 6318–6324 (2012)
63. S. Fremy, S. Kawai, R. Pawlak, Th. Glatzel, A. Baratoff, E. Meyer, Nanotechnology **23**, 055401 (2012)
64. R. Pawlak, Th Glatzel, V. Pichot, L. Schmidlin, S. Kawai, S. Fremy et al., Nano Lett. **13**, 5803–5807 (2013)
65. N. Fournier, C. Wagner, C. Weiss, R. Temirov, F.S. Tautz, Phys. Rev. B **84**, 035435 (2011)
66. N. Hauptmann, F. Mohn, L. Gross, G. Meyer, T. Frederiksen, R. Berndt, New. J. Phys. **14**, 073032 (2012)

67. C. Chiutu, A.M. Sweetman, A.J. Lakin, A. Stannard, S. Jarvis, L. Kantorovich et al., Phys. Rev. Lett. **108**, 268302 (2012)
68. A. Sweetman, S.P. Jarvis, H. Sang, I. Lekkas, P. Rahe, Y. Wang et al., Nat. Commun. **5**, 3931 (2014)
69. C. Lotze, M. Corso, K.J. Franke, F. von Oppen, J.I. Pascual, Science **338**, 779 (2012)
70. J. Repp, G. Meyer, S.M. Stojkovic, A. Gourdon, C. Joachim, Phys. Rev. Lett. **94**, 026803 (2005)
71. J. Repp, G. Meyer, S. Paavilainen, F.E. Olsson, M. Persson, Science **312**, 1196 (2006)
72. M.Z. Baykara, T.C. Schwendemann, E.I. Altman, U.D. Schwarz, Adv. Mater. **22**, 2838 (2010)
73. M. Abe, Y. Sugimoto, T. Namikawa, K. Morita, N. Oyabu, S. Morita, Appl. Phys. Lett. **90**, 203103 (2007)
74. S. Kawai, T. Glatzel, S. Koch, A. Baratoff, E. Meyer, Phys. Rev. B **83**, 035421 (2011)
75. J.E. Sader, S.P. Jarvis, Appl. Phys. Lett. **84**, 1801 (2004)
76. F.J. Giessibl, Phys. Rev. B **56**, 16010 (1997)
77. U. Dürig, Appl. Phys. Lett. **76**, 1203 (2000)
78. F.J. Giessibl, Appl. Phys. Lett. **78**, 123 (2001)
79. B. Such, T. Glatzel, S. kawai, S. Koch, E. Meyer, J. Vac. Sci. Technol. **B 29**, C4B1 (2010)
80. S. Sadewasser, T. Glatzel, *Kelvin Probe Force Microscopy: Measuring and Compensating Electrostatic Forces* (Springer, Berlin, 2012)
81. L. Nony, A.S. Foster, F. Bocquet, C. Loppacher, Phys. Rev. Lett. **103**, 036802 (2009)
82. F. Bocquet, L. Nony, C. Loppacher, Phys. Rev. B **83**, 035411 (2011)
83. A. Sadeghi, A. Baratoff, S.A. Ghasemi, S. Goedecker, T. Glatzel, S. Kawai et al., Phys. Rev. B **86**, 075407 (2012)
84. J. Tersoff, D.R. Hamann, Phys. Rev. Lett. **50**, 1998–2001 (1983)
85. J. Tersoff, D.R. Hamann, Phys. Rev. B **31**, 805–13 (1985)
86. S.A. Burke, J.M. Mativetsky, R. Hoffmann, P. Grütter, Phys. Rev. Lett. **94**, 096102 (2005)
87. L. Gross, F. Mohn, N. Moll, B. Schuler, A. Criado, E. Guitian, A. Diego Pena, A. Gourdon, G. Meyer. Science **337**, 1326–1329 (2013)
88. A.J. Weymouth, T. Hofmann, F.J. Giessibl, Science **343**, 1120–1122 (2014)
89. K. Boukari, P. Sonnet, E. Duverger, Chem. Phys. Chem. **13**, 3945–3951 (2012)
90. S. Kawaia, M. Koch, E. Gnecco, A. Sadeghi, R. Pawlak, T. Glatzel et al., Proc. Natl. Acad. Sci. USA **111**, 3968–3972 (2014)
91. L. Grill, M. Dyer, L. Lafferentz, M. Persson, M.V. Peters, S. Hecht, Nat. Nanotechnol. **2**, 687–691 (2007)
92. N.A.A. Zwaneveld, R. Pawlak, M. Abel, D. Catalin, D. Gigmes, D. Bertin et al., JACS **130**, 6678–6679 (2008)
93. L. Lafferentz, F. Ample, H. Yu, S. Hecht, C. Joachim, L. Grill, Science **323**, 1193 (2009)
94. W.A. Steele, Surf. Sci. **36**, 317–357 (1973)
95. R. Pawlak et al., submitted
96. S. Fremy et al., submitted